JOURNAL OF MATERIALS SCIENCE 33 (1998) 841–851

Numerical and experimental contact analysis of a steel ball indented into a fibre reinforced polymer composite material

K. VÁRADI, Z. NÉDER
Institute of Machine Design, Technical University of Budapest, H-1521 Budapest, Hungary
E-mail: varadik@eik.bme.hu

J. FLÖCK, K. FRIEDRICH
Institut für Verbundwerkstaffe GmbH (IVW), University of Kaiserslautern, 67663, Kaiserslautern, Germany
E-mail: friedrich@ivw.uni-kl.de

A three-dimensional anisotropic contact algorithm has been developed to analyse the contact behaviour of metal–composite bodies. The elements of the influence matrix are obtained by coupled finite-element anisotropic models. Linear elastic and approximate elastic–plastic techniques can evaluate the contact parameters (the normal approach, the size of the contact area and the contact pressure distribution) following different failure criteria. The contact technique is applied to the problem of a steel ball indented into a polymer composite material having either normal or parallel unidirectional fibre orientation. Finally, the contact results are verified by experimental evaluations. The latter were obtained by the use of a static testing machine, a laser profilometer, an optical microscope and a scanning electron microscope, and they illustrate the real response of the composite structure subjected to ball indentation. Good agreement between both methods could be demonstrated. © *1998 Chapman & Hall*

1. Introduction

The ball indentation test is a well-known procedure to evaluate the strength properties of metals in both the elastic and the elastic–plastic range. In recent years, this test has also been applied to anisotropic composite materials, in particular to characterize their mechanical behaviour, e.g., with regard to their fibre–matrix interfacial shear strength. The interfacial failure due to the indentation test was studied by Carman *et al.* [1] using experimental and analytical techniques. Microstresses were evaluated by macroscopic and microscopic approaches and a cellular modelling concept. According to their experimental observations, substantial fibre–matrix interfacial failure was found to occur underneath the ball indenter. To analyse the ball–composite contact problem, they obtained a solution with a macroscopic and microscopic approach utilizing an elasticity solution to formulate the macroscopic solution. Using the macroscopic solution to generate local boundary conditions in conjunction with a microscopic solution based on a cellular model, they constructed approximate closed-form solution for the stress state in a microregion.

To solve anisotropic contact problems, transversely isotropic solutions were presented by Dohan and Zarka [2], Gladwell [3], Suemasu *et al.* [4], Svelko [5] and Ovaert [6]; in all these cases, the plane of isotropy was oriented normal to the plane of contact.

The aim of this paper is to present a new anisotropic contact algorithm for the case where a composite material, containing normal (N) or parallel (P) fibre orientation in the surface, is subjected to ball indentation (Fig. 1). The numerical contact algorithm follows the influence matrix approach (reviewed in [7]), while the anisotropic influence matrix is obtained by coupled finite-element (FE) models. The approximate coupling technique considers only the displacements along the coupled surfaces. While "multiscale" modelling [8] or the "global–local" analysis [9] techniques are more general procedures, the coupled solution provides a more realistic elastic deformation of the composite system in the vicinity of the contact area, and at the same time also the effect of the macrosystem is incorporated.

The numerical contact algorithm, developed initially for isotropic bodies having rough surfaces [10], takes into consideration the non-linear material behaviour of a composite structure, using an approximate approach.

The final aim of developing an anisotropic contact algorithm was to apply it for sliding contact analysis of metal–composite surfaces; in addition, effects of contact temperatures should be evaluated. For the FE analysis the COSMOS/M system (vl. 75) [11] was used.

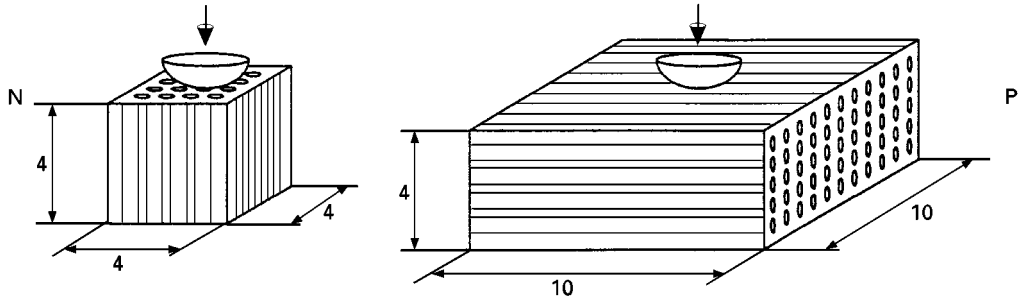

Figure 1 Specimens with the N and P fibre orientations.

The indentation problem was experimentally evaluated by measuring the force–displacement curve and by observing the indented areas using laser profilometry as well as optical microscopy and scanning electron microscopy (SEM).

The composite material (investigated under N and P fibre orientations) was a unidirectional continuous carbon fibre–poly(ether ether ketone) (PEEK) system, having a fibre volume fraction V_f of 0.6.

2. Contact algorithm, material properties and failure criteria

2.1. Anisotropic contact algorithm

The numerical contact algorithm is based on the influence matrix theory [7]. The elements of the influence matrix are obtained by FE modelling of a segment of the anisotropic 'half-space'.

2.1.1. Elastic case

To solve the contact problem, first the examined contact area should be discretized according to Fig. 2. The analysed contact area is divided into $(N-1)\times(M-1)$ rectangles with sizes of $2A\times 2B$. The contact parameters will be assigned to the corner points of the rectangles. They are denoted by row and column indices. The contact pressure distribution is divided into pressure segments acting over the small rectangles located around the corner points. As two examples, a unit pressure is applied at point k, l and a contact area, A_r, is composed by using five pressure segments (the z axis represents the direction and magnitude of the contact pressure).

To start with, both rough surfaces should be discretized and brought into a single point initial contact. The initial gaps h_{ij} can be assigned to each pair, while $u_{ij}^{(1)}$ and $u_{ij}^{(2)}$ are the elastic displacemets of body 1 and body 2 due to the contact pressure distribution. The sum of the initial gaps of both bodies is h_{ij} relative to the single point contact.

According to the geometric conditions of contact, the sum of the initial gap and the elastic displacements at the points of the real contact area A_r are equal to the normal (distance) approach, δ (in the following equations, δ_{ij} is assigned to the discretized points), while outside A_r they are greater:

$$\delta_{ij} = h_{ij} + (u_{ij}^{(1)} + u_{ij}^{(2)}) \quad \text{(over the contact area)} \tag{1a}$$

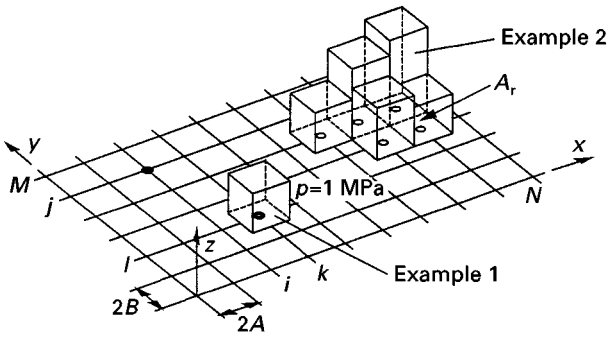

Figure 2 Theoretical illustration of contact pressure distribution on a discretized surface.

$$\delta_{ij} < h_{ij} + (u_{ij}^{(1)} + u_{ij}^{(2)}) \quad \text{(outside the contact area)} \tag{1b}$$

The stress conditions of contact express the fact that the acting pressures inside the contact area are greater than zero; at the same time, no pressure exists outside and along the borders of the contact area:

$$p_{ij} > 0 \quad \text{(over the contact area)} \tag{2a}$$

$$p_{ij} \equiv 0 \quad \text{(outside the contact area)} \tag{2b}$$

To fulfil these conditions, the contact pressure distribution, i.e., its location and magnitude, should be evaluated for a given normal approach and an initial gap field.

The relationship between the pressure and elastic displacement can be formed in the following way. The displacement of point i, j of body 1 due to the unit pressure acting around point k, l is $w_{ijkl}^{(1)}$ (Fig. 2). The total displacement of point i, j due to the continuously acting pressure segments is then

$$u_{ij}^{(1)} = \sum_{k=1}^{N}\sum_{l=1}^{M} w_{ijkl}^{(1)} p_{kl} \quad (i=1,\ldots,N) \quad (j=1,\ldots,M) \tag{3}$$

A similar equation may be formed for body 2. Substituting these two equations into Equation 1a leads to

$$\delta_{ij} = h_{ij} + \sum_{k=1}^{N}\sum_{l=1}^{M} w_{ijkl} p_{kl} \quad (i=1,\ldots,N) \quad (j=1,\ldots,M) \tag{4}$$

where

$$w_{ijkl} = w_{ijkl}^{(1)} + w_{ijkl}^{(2)} \tag{5}$$

2.1.2. Elastic–plastic case

The technique described so far assumed elastic deformation only, although at higher loads plastic deformations can occur. Therefore, assuming that the highest pressure possible is the plastic limit pressure p^*, the following step should be considered during the iteration process at step n:

$$\text{if } p_{ij}^n > p^*, \quad \text{then} \quad p_{ij}^n \equiv p^* \tag{6}$$

In this case the contact area has a plastic part surrounded by an elastic part.

The elastic–plastic forms of Equations 1a and 1b are as follows:

$$\delta_{ij} > h_{ij} + (u_{ij}^{(1)} + u_{ij}^{(2)}) \quad \text{(over the plastic contact area)} \tag{7a}$$

$$\delta_{ij} = h_{ij} + (u_{ij}^{(1)} + u_{ij}^{(2)}) \quad \text{(over the elastic contact area)} \tag{7b}$$

$$\delta_{ij} < h_{ij} + (u_{ij}^{(1)} + u_{ij}^{(2)}) \quad \text{(outside the contact area)} \tag{7c}$$

The stress-type contact conditions are

$$p_{ij} \equiv p^* \quad \text{(over the plastic contact area)} \tag{8a}$$

$$0 < p_{ij} < p^* \quad \text{(over the elastic contact area)} \tag{8b}$$

$$p_{ij} \equiv 0 \quad \text{(outside the elastic contact area)} \tag{8c}$$

Equation 7a expresses a contradiction, namely, that the displacements were obtained by elastic calculation over both the elastic and the plastic area. The locations of the elastic contact area and the elastic part of the pressure distributions are exact results. Furthermore, the plastic contact areas are always inside the elastic contact areas. The error of this approximation was analysed in [3] for an isotropic material by the help of a FE elastic–plastic model. The contact pressure maximum, the contact area and the normal approach showed good agreement when comparing the present technique with a non-linear FE analysis for two spheres over a wide range of plastic deformation.

2.1.3. Anisotropic influence matrix and multiple coupled finite-element models

To obtain the influence matrix for a certain composite material, first the anisotropic material properties must be calculated and assigned to the FE model. The latter represents a quarter of the total segment because of symmetry reasons (Fig. 3).

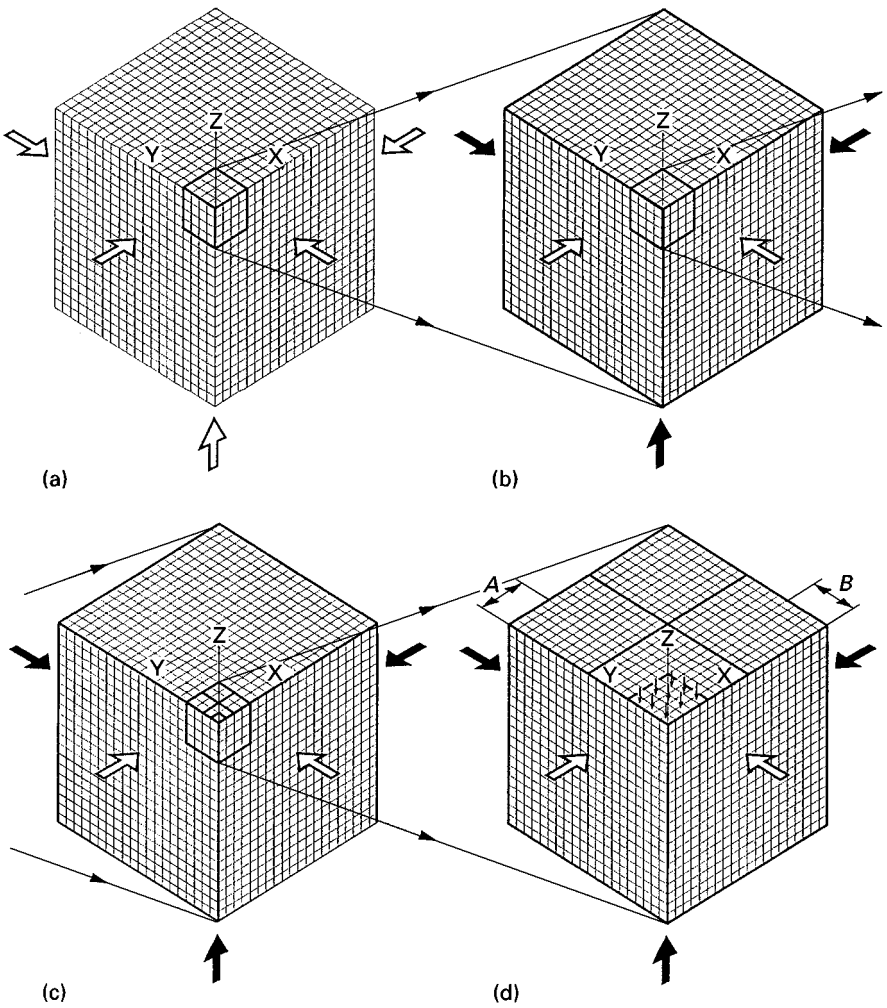

Figure 3 FE models and the coupling technique showing (a) step 1, (b) step 2, (c) step 3 and (d) step 4. (↙), coupled surface; (↗), zero prescribed displacement perpendicular to the surface.

The contact between two bodies produces predominantly local deformations and stresses, so that a smaller portion of the half-space is sufficient to be modelled. To obtain accurate results and to involve a fairly large part of the half-space, an approximate displacement coupling technique is used; it also allows one to obtain the elements of the anisotropic influence matrix. Fig. 3d shows the final FE mesh of a quarter segment together with the discretization of $2A \times 2B$ for the contact algorithm. Fig. 3c locates this segment in a larger model by coupling the displacements along the connecting side surfaces (i.e., the displacements of the points of the larger model, located at the boundary area of the smaller model, are assigned to the smaller model as boundary conditions all over its side surfaces). In the multiple coupled model, two further larger segments are used for increasingly larger portions of the elastic anisotropic half-space.

There is an approximation in the coupling technique. In step 4 (Fig. 3d) the pressure segment is acting on 5×5 elements as a constant unit pressure. In step 3 the unit pressure is acting on one element next to the origin of the coordinate system. In step 2 and step 1 the pressure is acting on one element while the magnitude of the pressure is proportionally smaller to transfer the same total force. Owing to the Saint Venant principle this approximation produces a small error along the coupled surfaces.

2.1.4. Accuracy of the coupling technique

The accuracy of the coupling technique was checked by the following series of two-dimensional problems. Fig. 4 shows two elastic half-segments, made of steel each with the size $500\,\mu m \times 500\,\mu m$, subjected to a concentric load of 1 N (acting on the half-model). In Fig. 4a the (not presented) FE mesh of model Pr1 contains 15 625 elements. The size of the smallest element is $1\,\mu m \times 1\,\mu m$. The model is fixed along three sides. In Fig. 4b the steps of the displacement coupling technique are shown. Model Pr2 has a uniform mesh of 20×20 elements and it is fixed along three sides. Model Pr3, also containing 20×20 elements, is "built into" Pr2 by coupling the displacements along the border of Pr3. Finally model Pr4, also containing 20×20 elements, is "built into" Pr3 by coupling the displacements along the border of Pr4. The calculated displacements are listed in Table I for each model. After the second coupling, models Pr2 + Pr3 + Pr4 produced almost the same maximum displacement as model Pr1, while model Pr2 and also Pr2 + Pr3 produced lower maximum displacements.

In the following calculations, the elements of the influence matrix are always obtained by the multiple coupling technique presented.

2.2. Material properties

The material properties for the ball and the composite material are listed in Table II assuming anisotropic fibre properties. The principal directions of the material are shown in Fig. 5. Transversely isotropic material properties were assumed for the composite material, calculated by "rule-of-mixtures" types of equation [12].

2.3. Failure criteria for ball indentation

Discussing the failure criteria for metal–composite contact problems requires further experimental and theoretical investigations. The following statements should be considered as "first" ideas, in this respect.

2.3.1. Failure in the case of normal fibre orientation

If the fibres have the N-orientation, failure of the composite due to ball indentation can occur by matrix deformation, interlaminar shear and compressive damage including fracture of the fibres.

To specify a pressure limit at which the interlaminar shear strains exceed a critical value requires further analysis of the behaviour of the composite structure. According to [1], initiation of failure starts below the surface followed by subsequent crack propagation to the surface.

To control the compression damage of the fibres their longitudinal compressive strength $\sigma^*_{\|C}$ should be

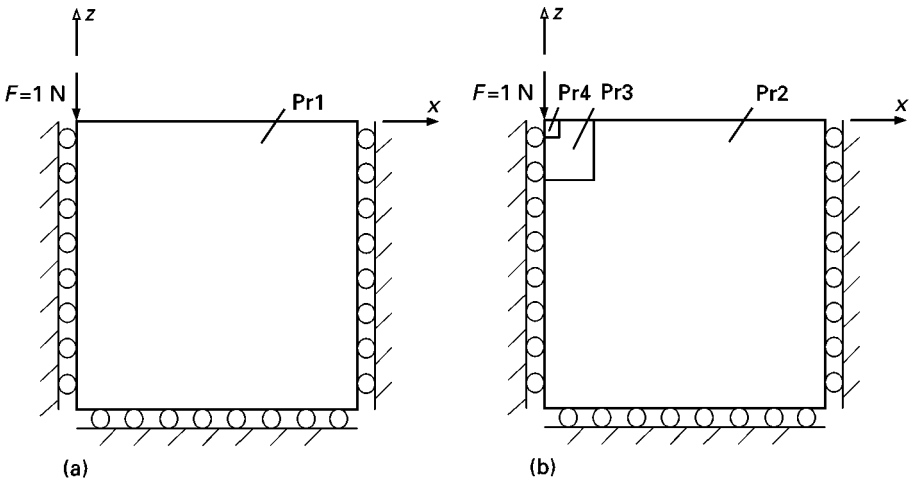

Figure 4 Testing the accuracy of the displacement coupling technique.

TABLE I Comparing the accuracy of the coupling technique

Model	Size of the smallest element (μm)	Number of elements	$u_{z\max}$ (mm)
Pr1	1	15 625	-3.671×10^{-5}
Pr2	25	400	-1.896×10^{-5}
Pr2 + Pr3	5	2×400	-2.759×10^{-5}
Pr2 + Pr3 + Pr4	1	3×400	-3.622×10^{-5}

TABLE II Anisotropic material properties assuming anisotropic fibre properties ($V_f = 0.6$)

Parameter (units)	Value for the following			
	Steel ball	Carbon fibre [13]	Matrix (PEEK) [13]	Composite (XC-2) [14]
E_{11} (MPa)	210 000	235 000		142 440
E_{22} (MPa)		15 000	3600	6618
E_{33} (MPa)		15000		6618
G_{12} (MPa)		6432		2932
G_{13} (MPa)	80769	6432	1286	2932
G_{23} (MPa)		5357		2196
ν_{12}		0.166		0.26
ν_{13}	0.3	0.166	0.4	0.26
ν_{23}		0.4		0.507

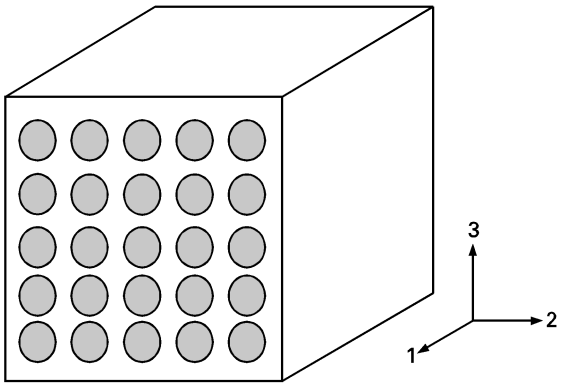

Figure 5 The principal directions of the material.

considered. This is an approximation, because the overall compression of a body and the local contact behaviour are not the same problem.

The condition of the longitudinal compressive strength may be considered as an upper limit for the vertical stresses inside the contact area. This condition does not allow any further plastic-type deformation. The contact failure-type criterion is therefore assumed to be

$$p^* = \sigma^*_{\|C} \tag{10}$$

2.3.2. Failure in the case of parallel fibre orientation

If the fibres have the P orientation, failure of the composite due to ball indentation relates primarily to plastic deformation of the matrix and flexural fracture of the fibres.

As a first-order approach, the transverse compressive strength $\sigma^*_{\perp C}$ may be considered as a yield strength-type criterion. The matrix can accumulate certain plastic deformation without any fracture-type failure. To approximate this type of behaviour, the plastic limit pressure conditions, similar to the contact of isotropic metals, are as follows [7]:

$$p^* = 1.6\sigma^*_{\perp C} \quad \text{(in the range of starting plastic deformation)} \tag{11a}$$

$$p^* = 3.0\sigma^*_{\perp C} \quad \text{(in the range of larger plastic deformation)} \tag{11b}$$

In Equations 11a and 11b, the factor of 1.6 represents the limit pressure that produce initial yielding below the contact area, while the factor of 3.0 represents more intensive plastic deformation in the vicinity of the contact area.

3. Experimental indentation studies

3.1. Test rig and deformations measured

A 100Cr6 steel ball having a diameter of 2 mm was indented into the surface of an XC-2 unidirectional carbon-fibre-reinforced PEEK system [14]. Tests were carried out by the use of a Zwick 1445 static testing machine. With this device it was possible to program defined load and loading rate levels. During the tests, loads, F, versus displacements, h, (same as for the normal approach, δ) were measured and recorded with an X–Y plotter. Fig. 6 shows a scheme of the testing configuration.

Before testing, the composite specimens were polished with diamond paste (3 μm) until smooth surfaces were achieved. To get reproducible results, it was important that the surfaces were prepared to be perpendicular to the loading direction.

Tests were carried out for the N and P fibre orientations. Six different loads were applied (10, 20, 30, 40, 50 and 100 N). The loading speed was 0.3 mm min^{-1}.

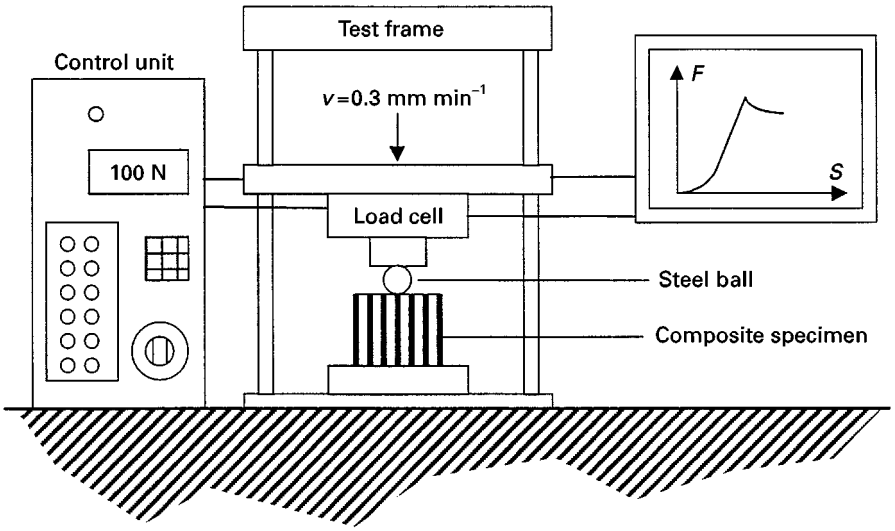

Figure 6 Scheme of the static testing device.

The measured total displacement represents the deformation of the whole system, i.e., that of the composite specimen, of the steel ball and of the frame of the testing machine. To get results that were relevant only to the contact deformation of the composite specimen and the steel ball, the deformation of the testing device was measured under the same loading conditions, but without the composite specimen and steel ball; both were replaced by a more rigid steel cube. The resulting deformation was used to correct the original measurement ("corrected deformation"), so as to achieve the amount of displacement that belonged to the local indentations of the steel ball and the composite sample only.

The results obtained are shown in Fig. 7 for both orientations, where the total deformation curves refer to the total measured indentation data (under load) and the corrected deformation curves refer to the results after subtracting the deformation of the testing device (under load).

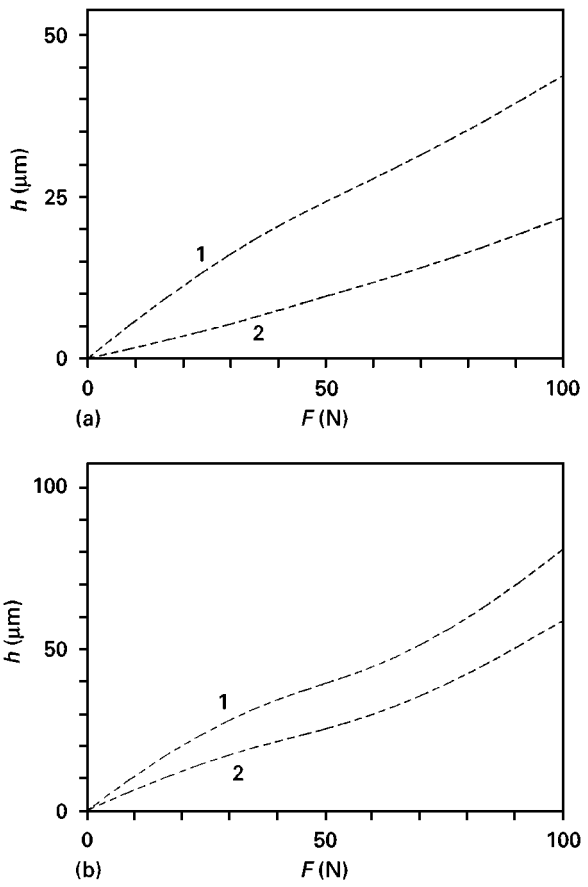

Figure 7 Measured force–displacement values during ball indentation tests for (a) the N fibre orientation and (b) the P fibre orientation. Curves 1, total deformation; curves 2, corrected deformation.

3.2. Diameter of the effective and the residual contact areas

During the indentation test the steel ball is compressed into the composite structure (Fig. 8). Assuming a rigid ball, the maximum deformation, h, of the composite specimen is equal to the "corrected deformation" (explained in Section 3.1). Fig. 8 represents the deformation of this structure showing the diameter $2r_{\text{eff}}$, of the real contact area and also $2r^*_{\text{eff}}$ as an upper limit of $2r_{\text{eff}}$. Based on trigonometric expressions the upper limit $2r^*_{\text{eff}}$ is

$$2r^*_{\text{eff}} = 2[h(D - h)]^{1/2} \tag{12}$$

The evaluated effective contact diameters $2r^*_{\text{eff}}$ are shown in Fig. 9a and b for N and P fibre orientations, respectively; the calculated curves refer to the effective contact diameter as calculated from the measured corrected indentation depth values. Furthermore these results are compared with direct measurements of the remaining indentations by the use of both reflected optical microscopy (Fig. 10) and laser profilometry (Fig. 11). Both the latter results represent the unloaded state (as a residual indentation marker), proving that local failure events must have occurred besides the elastic deformation of the bodies (see Section 2.3); otherwise after unloading there would not be such dominant residual contact areas visible at every load level.

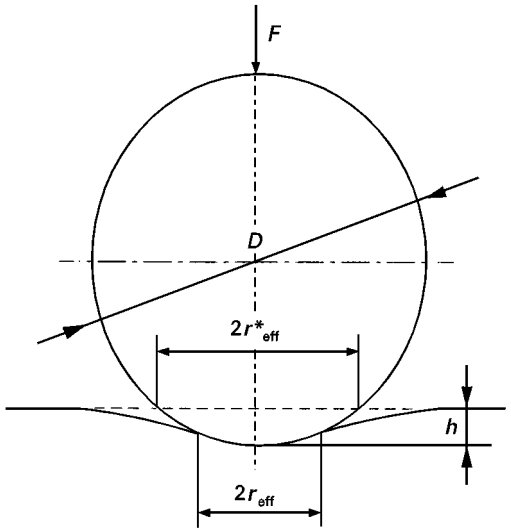

Figure 8 Sketch of the ball indentation test.

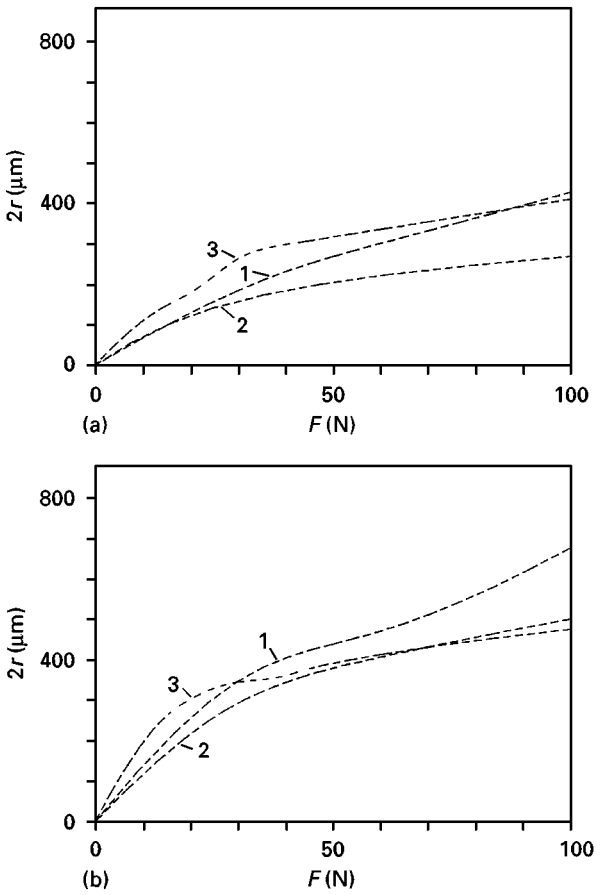

Figure 9 Experimental results for the effective and residual diameters of the contact area for (a) the N fibre orientation and (b) the P fibre orientation. Curves 1, calculated from corrected deformation ($2r^*_{\mathrm{eff}}$, effective); curves 2, laser profilometer ($2r_{\mathrm{l}}$, residual) curves 3, optical microscopy ($2r_{\mathrm{m}}$, residual).

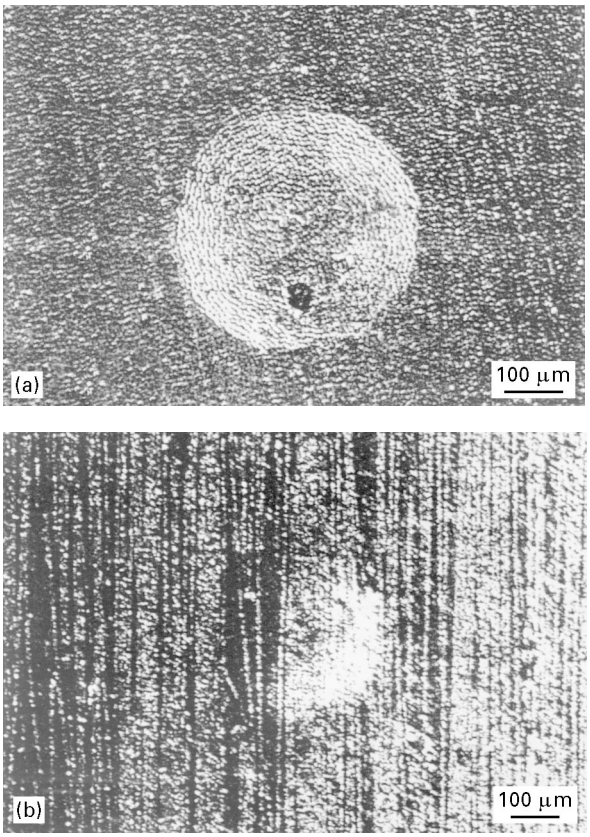

Figure 10 The residual indented area observed by optical microscopy for (a) the N fibre orientation ($F = 100$ N) and (b) P fibre orientation ($F = 40$ N).

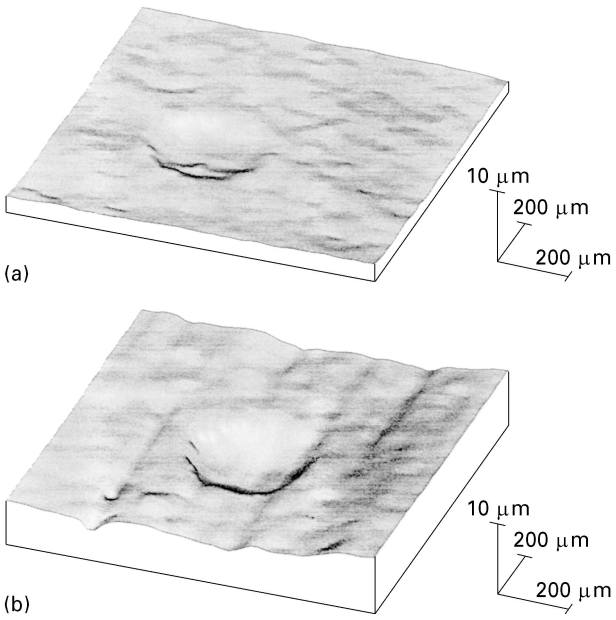

Figure 11 The residual indented area evaluated by laser profilometry for (a) the N fibre orientation ($F = 100$ N) and (b) P fibre orientation ($F = 40$ N).

According to Figs 8 and 12, $2r^*_{\mathrm{eff}}$, as an upper limit, is much larger than $2r_{\mathrm{eff}}$. Considering only the tendencies, one may assume that the size of the unknown effective contact diameter, $2r_{\mathrm{eff}}$ is about 50–70% of the size of the calculated diameter, $2r^*_{\mathrm{eff}}$.

As an example, the profiles of the effective and the residual contact areas, as measured for the parallel fibre orientation and a load $F = 50$ N, are shown in Fig. 12. In the loaded state, the deformation is much larger than the residual deformation. At the same time the different diameters of the contact areas (effective deformed, $2r^*_{\mathrm{eff}}$ and residual, $2r_{\mathrm{m}}$ or $2r_{\mathrm{l}}$) are in the same range.

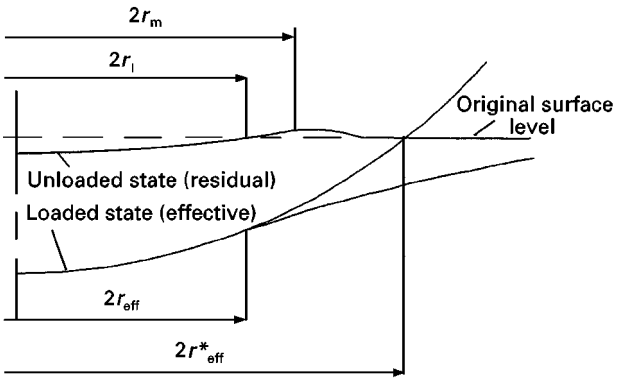

Figure 12 The profile of the effective and the residual contact areas for $F = 50$ N in the P fibre orientation ($2r_m$, diameter of the residual contact area by optical microscopy; $2r_l$ diameter of the residual contact area by laser profilometry).

3.3. Damage during indentation

SEM was used to determine the local damage of the composite specimens due to steel ball indentation. Every specimen was coated with a thin gold layer in order to avoid electrical charging effects on the surface. The gold layer had a thickness of 20 nm. The indentations were observed at an angle of 53°, at which the best contrast was achieved.

For the P fibre orientation no cracking of fibres or matrix was detected. The specimens showed only a shallow indentation, into which the fibres were mainly bent in the direction of indentation, but were almost not perpendicular to it.

For the N orientation of the fibres, some sites of damage could be observed. In particular at the edges of the indentation there was a slight debonding and cracking of the fibres. Failure of the fibre–matrix interfaces was also detectable. Of course most of the plastic deformation had occurred in the softer matrix, which was also visible in the different "height levels" of the fibres and the matrix.

In both cases, the P and the N fibre orientation, the indentation showed almost the shape of a circle which is, however, not visible on the SEM photographs owing to the necessary tilting angle.

Fig. 13a illustrates for the N fibre orientation that compressive damage of fibre ends (in the form of cracks across a section of the fibre diameter) had occurred during the indentation test.

Fig. 13b shows the indented area in the case of the P fibre orientation.

4. Numerical contact analysis

The contact results were evaluated with regard to the following parameters: normal approach; δ; length of the contact area, $2a$; width of the contact area, $2b$; maximum contact pressure, p_{max}.

Contact calculation for coupled models with N and P fibre orientations are presented. The composite material evaluated was XC-2 (see Table II).

To be able to verify numerically the experimental contact results, calculations were carried out for a higher load level (10–100 N). Here the size of the contact area was in the range 0.1–1 mm. Following the multiple coupled model idea, the FE influence matrix was obtained according to the FE models listed in Table III.

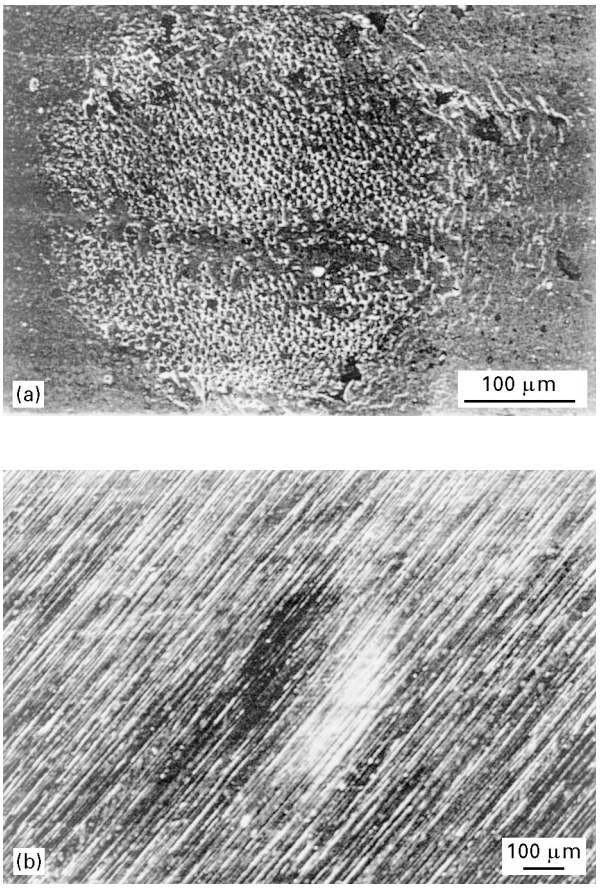

Figure 13 The residual indented area by scanning electron microscopy for (a) the N fibre orientation ($F = 100$) and (b) the P fibre orientation ($F = 40$).

TABLE III The size of the multiple coupled FE models

Step	FE model size μm	FE element size μm
1	2500 × 2500 × 2500	125 × 125 × 125
2	500 × 500 × 500	25 × 25 × 25
3	100 × 100 × 100	5 × 5 × 5
4	20 × 20 × 20	1 × 1 × 1

The size of the "unit cell" in the contact algorithm was $2A \times 2B = 10\,\mu m \times 10\,\mu m$.

4.1. Elastic results

Table IV presents the elastic results achieved with the multiple coupled models for the N orientation, whereas Table V contains those for the P orientation. In the latter case, $2a$ represents the length of the contact area in fibre direction.

In the higher load range the calculated maximum contact pressure values are above the limit strength values of the composite materials for both fibre orientations. This means that the linear elastic contact algorithm can give only approximate results for δ, $2a$ and $2b$. Therefore, various failure criteria should be considered.

TABLE IV Contact parameters: elastic results with multiple coupled models for the N orientation

Parameter (units)	Value for the following loads			
	10 N	20 N	50 N	100 N
δ (μm)	3.81	5.98	10.79	16.80
$2a$ (μm)	130	170	230	270
$2b$ (μm)	130	170	230	270
p_{max} (MPa)	1197	1495	2033	2616

TABLE V Contact parameters: elastic results with multiple coupled models for the P orientation

Parameter (units)	Value for the following loads			
	10 N	20 N	50 N	100 N
δ (μm)	10.14	15.98	29.12	45.76
$2a$ (μm)	190	250	330	430
$2b$ (μm)	230	270	370	470
p_{max} (MPa)	457	576	791	1002

To check the accuracy of the anisotropic contact algorithm, FE contact models were created for the ball indentation problem in the case of both fibre orientations. They led, in fact, to similar results as shown here. Details have been presented in [15].

4.2. Approximate elastic–plastic results

In Section 2.3, different failure criteria were reviewed for ball indentation tests. For the case of the N orientation a value of $\sigma^*_{\parallel C} = 1100$–$2600$ MPa was found in the literature [13]. According to this reference, the contact failure pressure for the present material was chosen to be

$$p^* = \sigma^*_{\parallel C} = 1200\,\text{MPa}$$

Using this limit pressure condition leads to elastic–plastic contact results given in Table VI.

In the case of the P orientation, the compressive strength for material XC-2 would be in the range of $\sigma^*_{\perp C} = 192$–253 MPa [13]. Choosing $\sigma^*_{\perp C} = 220$ MPa for the present case, the plastic limit pressure conditions are:

$$p^* = 1.6\sigma^*_{\perp C} \approx 350\,\text{MPa}$$

$$p^* = 3.0\sigma^*_{\perp C} \approx 660\,\text{MPa}$$

respectively.

The first limit condition ($1.6\,\sigma^*_{\perp C}$) represents the initial phase of local plastic deformation in the matrix, while the second condition ($3.0\sigma^*_{\perp C}$) represents plastic deformation extended over a wider region, containing several fibres embedded in the surrounding matrix mateial.

The results of the approximate elastic–plastic contact algorithm are listed in Tables VII and VIII. By comparing Tables V, VII and VIII, almost the same results are achieved as long as $F \leqslant 10$ N; the differences above this load level are due to the plastic shear deformation processes occurring in the vicinity of the contact area of the polymer composite material during ball indentation.

TABLE VI Contact parameters: elastic–plastic results with multiple coupled models for the N orientation ($p^* = \sigma^*_{\parallel c}$)

Parameter (units)	Value for the following loads			
	10 N	20 N	50 N	100 N
δ (μm)	3.81	6.05	11.68	19.97
$2a$ (μm)	130	170	250	330
$2b$ (μm)	130	170	250	330
p_{max} (MPa)	1197	1200	1200	1200

TABLE VII Contact parameters: elastic–plastic results with multiple coupled models for the P orientation ($p^* = 1.6\,\sigma^*_{\perp c}$)

Parameter (units)	Value for the following loads			
	10 N	20 N	50 N	100 N
δ (μm)	10.31	17.08	33.02	61.93
$2a$ (μm)	210	270	430	610
$2b$ (μm)	230	290	450	630
p_{max} (MPa)	350	350	350	350

TABLE VIII Contact parameters: elastic–plastic results with multiple coupled models for the P orientation ($p^* = 3.0\,\sigma^*_{\perp c}$)

Parameter (units)	Value for the following loads			
	10 N	20 N	50 N	100 N
δ (μm)	10.14	15.98	29.31	47.80
$2a$ (μm)	190	250	350	450
$2b$ (μm)	230	270	370	490
p_{max} (MPa)	457	576	660	660

4.3. Comparison of calculated and measured results

The results of the elastic and approximate elastic–plastic contact calculations are compared in Figs 14 and 15 with the measured values. In Figs 14a and 15a the measured displacements, h, and the calculated normal approach, δ, are the same parameters. In Figs 14b and 15b the diameter, $2r$, of the measured indentations is compared with the calculated length, $2a$, of the contact area.

For the N fibre orientation the results are collected in Fig. 14. Considering the indentation results, the normal approach δ shows higher values for the elastic-plastic (curve 12) in comparison with the elastic contact calculation (curve 11 in Fig. 14a). The measured corrected results for the normal approach (curve 2) exhibit slightly smaller values in the lower load range, whereas they are in between the two theoretical curves 11 and 12 for the higher load range.

The measured size of the contact area is represented by curves 1 to 3 in Fig. 14b. The calculated elastic (curve 11) and elastic–plastic (curve 12) contact lengths, $2a$, are almost in the same range. As the

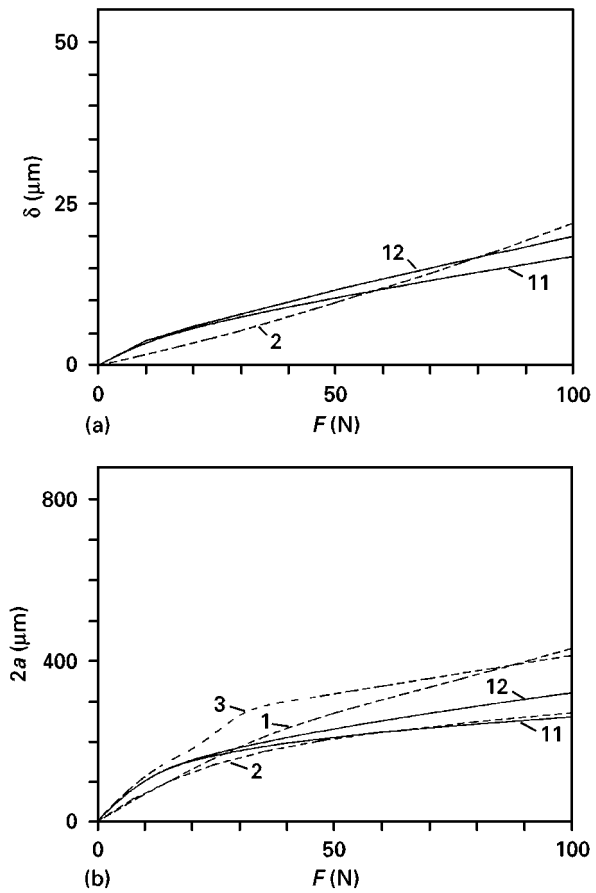

Figure 14 (a) The normal approach (curve 2, corrected deformation) and (b) the size of the contact area for the *N* orientation (curve 1, calculated from corrected deformation; curve 2, laser profilometer; curve 3, optical microscopy; curve 11, contact analysis, result (elastic) curve 12, contact analysis result elastic–plastic; $p^* = \sigma_{\|}^*$).

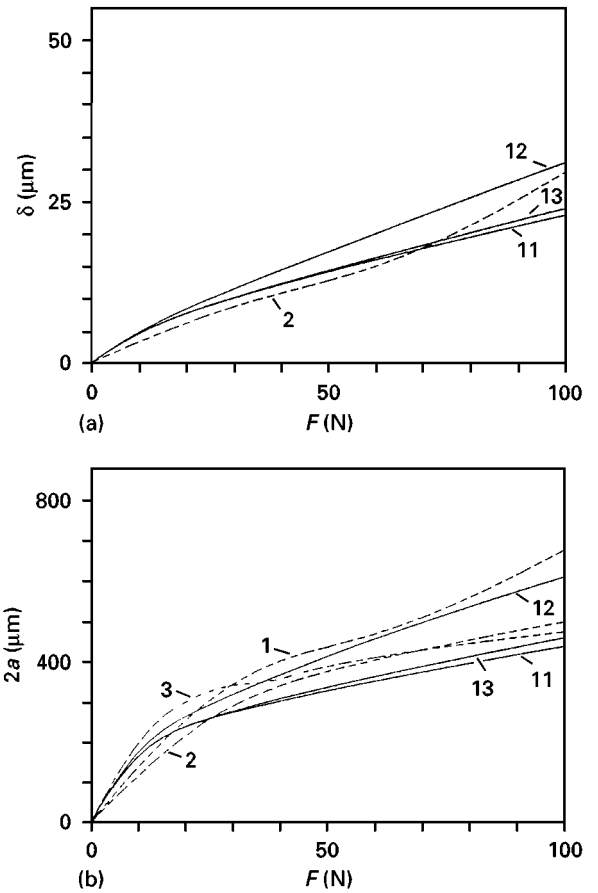

Figure 15 (a) The normal approach (curve 2, corrected deformation) and (b) the size of the contact area for the P orientation (curve 1, calculated from corrected deformation; curve 2, laser profilometer; curve 3, optical microscopy; curve 11, contact analysis result (elastic); curve 12, contact analysis result (elastic–plastic; $p^*1.6\sigma_{\|C}^*$); curve 13 contact analysis result (elastic–plastic; $p^*3.0\sigma_{\|C}^*$).

effective contact area is always greater than the residual contact area, curves 2 and 3 are the most reliable experimental results. As expected, the calculated elastic–plastic results (curve 12) are in the best agreement with the measured data.

For the P fibre orientation the results are collected in Fig. 15. Curve 12 represents the calculated initial phase of plastic deformation that appears at a load level of about 10–20 N. At a higher load level, curve 13 represents a more intensive plastic deformation. The elastic contact calculation (curve 11) produced slightly smaller values. The corrected measured deformation (curve 2) is in the range of curves 11 and 13.

The size of the contact area is represented by curves 1–3 in Fig. 15b. The calculated results of curve 12 represent again the initial phase of the plastic deformation, while curve 13 represents a more intensive plastic deformation. The elastic solution (curve 11) resulted again in the smallest values. If the effective contact area is greater than the residual contact area, one may accept that curves 2 and 3 are the most useful experimental results for a comparison. The calculated contact results (curve 13) are then almost in the range of the measured results (curves 2 and 3).

5. Conclusions

1. The displacement coupling technique applied provides reliable displacement results, considering that an elastic material surrounds the small FE models.

2. The shape of the contact area for the N fibre orientation is obviously circular while for the P fibre orientation it is slightly elliptical.

3. At a higher load level in the case of both fibre orientations the linear elastic material law cannot describe the behaviour of the composite structures subjected to the ball indentation test. The approximate elastic–plastic contact technique gives better results. This approach requires more accurate material properties for the composite structure and its FE elastic–plastic verification.

4. Rather good agreement could be achieved between experimentally determined ball indentation geometries and theoretically predicted geometries.

Acknowledgements

The presented research was sponsored by the Deutsche Forschungsgemeinschaft (DFG FR675/19-1) and by governmental agencies BMBF and OMFB as part of the German–Hungarian research co-operation on the contact mechanics of different materials.

References

1. G. P. CARMAN, J. J. LESKO, K. L. REIFSNIDER and D. A. DILLARD, *J. Compos. Mater.* **27** (1993) 303.
2. M. DOHAN and J. ZARKA, *Int. J. Solid Struct.* **13** (1977) 229.
3. G. M. L. GLADWELL, Contact problems in the classical theory of elasticity (Sitjthoff and Nordhoff, in Alpen ann den Rijn, 1980) pp. 575–631.
4. H. SUEMASU, S. KERTH and M. MAIER, *J. Compos. Mater.* **28** (1994) 1723.
5. V. A. SVELKO, *PPM J. Appl. Math. Mech.* **34** (1970) 172.
6. T. C. OVAERT, *J. Tribol.* **115** (1993) 650.
7. K. L. JOHNSON, "Contact mechanics" (Cambridge University Press, Cambridge, 1985).
8. M. W. BEALL, M. S. SHEPHARD, J. FISH and V. BELSKY, in 1996 ASME International Mechanical Engineering Congress and Exposition, 17–22 November 1996, Atlanta, Georgia (American Society for Mechanical Engineers, New York, 1996).
9. J. ZHANG, N. KIKUCHI and K. TERADA, in 1996 ASME International Mechanical Engineering Congress and Exposition, 17–22 November, 1996, Atlanta, Georgia (American Society for Mechanical Engineers, New York, 1996).
10. K. VÁRADI and Z NÉDER, *Tribologia* **3** (1996) 237.
11. "COSMOS/M user guide v1.75" (Structural Research and Analysis Corporation, 1995).
12. D. HULL, "An introduction to composite materials' (Cambridge University Press, Cambridge, 1990).
13. F. N. COGSWELL, "Thermoplastic aromatic polymer composites" (Butterworth–Heinemann, Oxford, 1992).
14. "Thermoplastic composite materials handbook" (ICI Thermoplastic Composites Inc., 1992).
15. K. VÁRADI, Z. NÉDER, K. FRIEDRICH and J. FLÖCK, *Compos. Sci. Technol.* (1997) submitted.

Received 15 August
and accepted 24 September 1997